AIP Advances

Study on the electrowetting and beam current characteristics of externally wetted ionic liquid electrospray thruster

Cite as: AIP Advances **11**, 125030 (2021); https://doi.org/10.1063/5.0069731
Submitted: 02 September 2021 • Accepted: 06 December 2021 • Published Online: 27 December 2021

Senwen Xue, Li Duan and Qi Kang

Study on the electrowetting and beam current characteristics of externally wetted ionic liquid electrospray thruster

Cite as: AIP Advances 11, 125030 (2021); doi: 10.1063/5.0069731
Submitted: 2 September 2021 • Accepted: 6 December 2021 •
Published Online: 27 December 2021

Senwen Xue, Li Duan, and Qi Kang[a]

AFFILIATIONS

Key Laboratory of Microgravity, Institute of Mechanics, Chinese Academy of Sciences, Beijing 100190, People's Republic of China and School of Engineering Sciences, University of Chinese Academy of Sciences, Beijing 100049, People's Republic of China

[a]Author to whom correspondence should be addressed: kq@imech.ac.cn

ABSTRACT

It is the theoretical basis to analyze the hydrodynamics mechanism of ionic liquid in an electrostatic field to ensure that the ionic liquid electrospray thruster possesses good wettability. Stable and continuous electrowetting emitters are closely related to thrust noise, resolution, and stability. Therefore, it is urgent to explore the law of ionic liquid electrowetting emitters in an electrostatic field to improve the performance of thrusters. The article proposes a new hybrid emitter structure, which consists of a V-blade emitter and a square capillary. It also carries out numerical simulation of emitter electrowetting under normal gravity and atmospheric conditions and emission experiments to explore the process of ionic liquid layer spreading on the external surface of the emitter. The dimensions of the emitter d_1, d_2, and θ and the physical properties of ionic liquids jointly determine the electrowetting velocity, the threshold of wetting voltage, and the liquid layer thickness. By analyzing the influence of various variables on electrowetting, a complete emitter electrowetting law of ionic liquid electrospray thrusters is summarized, which provides an important basis for the optimization of the emitter structure. Considering the scale of the emitter and bond ≈1, the meniscus in the electrostatic field is mainly affected by gravity, surface tension, viscous force, and electrophoretic force. Accordingly, it is worth noting that electrophoretic force is calculated by the Maxwell stress tensor method that treats ionic liquids as a dielectric to ensure the continuity of the meniscus. Although it can satisfy the electrowetting study at the macroscale, the interaction between anions and cations at the micro-scale is ignored. The numerical simulation results and the experimental results are correlated. It is proved that the method used in this article is accurate enough to simulate electrowetting before the liquid layer breaks up to form ion emission.

I. INTRODUCTION

Micro-electric propulsion technology occupies an important position in space missions such as orbit maintenance, attitude controlling, and formation flying of micro-nano-satellites (mass <100 kg).[1] As one of the most promising micro-electric propulsion technologies, the ILET (Ionic Liquid Electrospray Thruster) has a simple structure, which is easy to be integrated into arrays. It also can realize anionic and cationic emission modes so as to ensure the electrical neutrality of the aircraft without a neutralizer. The University of California has developed a hybrid emitter that consists of a capillary emitter with a protruding, coaxial needle. They find that a needle at the center of a capillary emitter can promote stable emission at a low flow rate in an externally wetted emission mode. When the flow rate is increased, the meniscus extends past the needle to emit in a capillary or cone-jet mode. Their emitter has produced emission at roughly 2 and 360–430 nA for externally wetted and capillary modes, respectively. Their electrospray thruster is capable of both a high specific impulse mode and a high thrust-to-power mode under separate operating conditions.[2]

Regardless of whether a capillary, porous medium or externally wetted surface is used to form an electrospray, the emitter geometry is selected to produce the desired performance. Early electrospray experiments utilized capillary emitters that must be

equipped with high precision micro-pumps and micro-valves, providing propellant pressure to the capillary tip. This type of emitter is represented by the CMNT from Busek and the Jet Propulsion Laboratory.[3,4] Salient among them is the broadly adjustable thrust from 5 to 30 μN with a maximum specific impulse of ~400 s. The specific impulse of the CMNT is low because emission produces a mixture of primarily droplets and low levels of ions, but its thrust resolution of <0.1 μN and thrust noise of <0.1μN Hz$^{-1/2}$ far meet the requirements of the ST7-DRS and LISA measurement bandwidths.[5–7]

On the contrary, externally wetted tungsten needles have a robust history of producing high specific impulse under ion-mode emission readily in the laboratory.[8] The liquid supply system is obviated in the externally wetted configuration, considerably reducing the ion source complexity. Active control within the ionic regime can be achieved by adjusting the temperature, which has a strong influence on viscosity, and the accelerating voltage through an adequate aperture electrode.[9] A fully integrated micro-fabricated externally wetted electrospray thruster from the Massachusetts Institute of Technology is an array of 502 emitters in a 113 mm^2 area with a total thrust of up to 13 μN and a 3000 s specific impulse under the pure ion-emission regime.[10] They find that the presence of sharp surface roughness features may allow formation of a conical liquid surface supported by the surface roughness, allowing high field enhancement and ion emission before the surface is destabilized into a Taylor cone.

The combination of high thrust chemicals and high specific impulse electric propulsion into a single multi-mode propulsion (MMP) system has the potential to greatly enhance spacecraft mission capability.[11] For example, plane change maneuvers are very costly in terms of the propellant required. Performing a plane change can quickly drain a spacecraft's propellant requirement. The utilization of an MMP system could greatly reduce the amount of propellant required for the maneuver.[12–14] MMP systems have been envisioned using electrospray propulsion for the high specific impulse component and cold gas thrusters[15] or monopropellant rockets[16] for the high thrust component.

This article proposes a new hybrid emitter structure, which consists of a V-blade emitter and a square capillary. The unique configuration ensures that the ILET can be used in both ion emission mode with a high specific impulse and droplet emission mode with a high thrust power ratio. The switching of two emission modes has a great relationship with emitter electrowetting. The thickness of the liquid layer on the externally wetted emitter surface determines the mass flow rate at the emitter tip that directly differentiates the emission mode. The configuration of the meniscus and the thickness of the liquid layer are determined by the electrostatic field, the scale of the structure, the material of the emitter, and the physical property of the ionic liquid jointly. Therefore, it is significant to research the law of hybrid emitter electrowetting for the performance evaluation of the ILET. Space missions such as formation flight of micro-nano-satellites and gravitational wave detection require high-performance electric propulsion systems to provide a superior thrust scheme that have advantages such as low noise, high resolution, high specific impulse, and a high thrust power ratio. The study of electrowetting and the relationship between electrowetting and beam current are a meaningful step to optimize the performance of the ILET.

II. SIMULATION MODEL OF HYBRID EMITTER

The traditional ILET structure is merely composed of an emitter and extractor, but the hybrid one adds a square capillary around the V-blade emitter. An electrostatic field is created between the square capillary and the extractor, in which the ionic liquid is treated as the dielectric. Gravity, surface tension, viscous force, and electrophoretic force work together to form a meniscus between the V-blade emitter and the square capillary. When the electrostatic field is strong enough, the ionic liquid will be able to climb up along the V-blade emitter to form a thin liquid layer that wetted the emitter all the way to the tip. As the intensity of the electric field gradually increases, ions, ion clusters, or charged droplets will break through the liquid energy barrier and form a stable cone jet at the tip. The composition of the cone jet is very complex. The different composition will determine whether the ILET operates in a pure ion mode with a high specific impulse, a droplet mixed with ions mode with a high thrust power ratio, or a pure droplet mode with a high thrust.[17] The emission mode is closely related to the thickness of the liquid layer at the tip. The configuration of the meniscus is influenced by the distance between the emitter and extractor, the diameter of the extractor hole, the contact angle between the material and the ionic liquid, the cone angle of the V-blade emitter, and the physical property of the ionic liquid, thus resulting in different liquid layer thicknesses.

The hybrid emitter is a symmetrical structure, and a two-dimensional model is selected for simulation under the atmosphere. The key variables and boundary conditions are shown in Fig. 1. Due to the existence of the square capillary, the hybrid emitter has a controllable flow to transport and manage the ionic fluid. It still retains the advantage of the traditional needle emitter with a very sharp tip, which makes the threshold of wetting voltage relatively lower. The variable d_1 is the aperture of the extractor. The variable d_2 is the distance from the V-blade emitter to the extractor. The variable θ is the angle of the V-blade emitter. The variable θ_w is the contact angle.

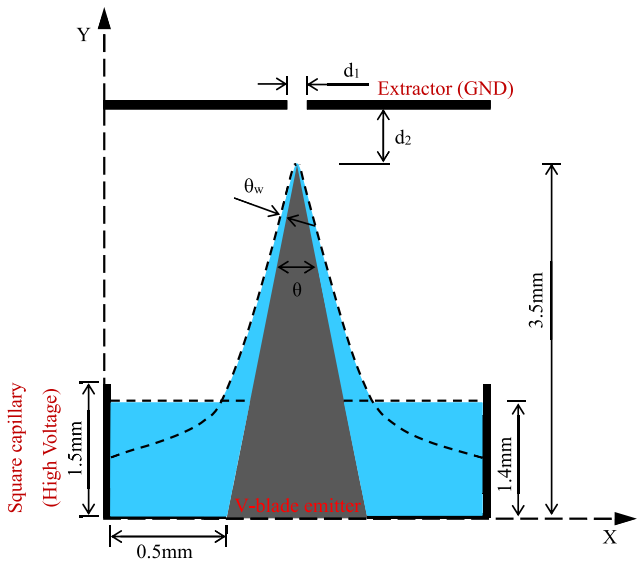

FIG. 1. Two-dimensional simulation model graph of the hybrid emitter.

TABLE I. The propellant properties (25 °C, 1 atm).

Abbreviation	μ (Pa s)	γ (N/m)	ρ (kg/m^3)	ε_r (l)	σ (S/m)
EMI-TFSI	0.034	0.023 67	1520	11.3219	0.92
EMI-BF4	0.042	0.042 73	1280	13.2381	1.36
EMI-DCA	0.021	0.044 53	1080	11.6593	1.8

Ionic liquids are a relatively new class of substances investigated especially for their peculiar electrochemistry.[18] Ionic liquids have negligible saturated vapor pressure and other unique properties. All salts obtain this state if heated to the proper temperature, but there is a subgroup known as room-temperature ionic liquids that can remain liquid at or below 293 K.[19] These physical properties ensure that the ionic liquid can infiltrate the emitter better. An ionic liquid is either an organic or inorganic salt in a molten (liquid) state. Because of its molten state, the cation and anion of the salt dissociate, but the overall liquid remains quasi-neutral. One of the polarities is extracted from the liquid surface, while the other stay and eventually discharge at the electrode. This has a direct detrimental effect over the performance and lifetime of the emitter. The damage of the emitter can be averted by using polarity alternation of the power supply at a typically low frequency dictated by the charging time of the double layer generated at the liquid–metal interface, which depends on the electrochemical window of the ionic liquid.[20] EMI-TFSI, EMI-BF4, and EMI-DCA are selected as the simulation and experimental media in this article, and the main physical properties are shown in Table I.

III. NUMERICAL SIMULATION

A. Physical field coupling

Since the fluid model of the ILET has a very small Reynolds number, the process of ionic liquid climbing along the outer surface of the emitter conforms to the laminar flow hypothesis, which can be described by the Navier–Stokes equation of incompressible fluid under constant viscosity, as follows:

$$\begin{cases} \dfrac{\partial v_x}{\partial x} + \dfrac{\partial v_y}{\partial y} = 0, \\ \dfrac{\partial v_x}{\partial t} + v_x\dfrac{\partial v_x}{\partial x} + v_y\dfrac{\partial v_x}{\partial y} = f_x - \dfrac{1}{\rho}\dfrac{\partial P}{\partial x} + \dfrac{\mu}{\rho}\left(\dfrac{\partial^2 v_x}{\partial x^2} + \dfrac{\partial^2 v_x}{\partial y^2}\right), \\ \dfrac{\partial v_y}{\partial t} + v_x\dfrac{\partial v_y}{\partial x} + v_y\dfrac{\partial v_y}{\partial y} = f_y - \dfrac{1}{\rho}\dfrac{\partial P}{\partial y} + \dfrac{\mu}{\rho}\left(\dfrac{\partial^2 v_y}{\partial x^2} + \dfrac{\partial^2 v_y}{\partial y^2}\right) + \rho g. \end{cases} \tag{1}$$

In Eq. (1), f_x and f_y are the volume force imposed on the ionic liquid, which is mainly composed of surface tension $\mathbf{F_{st}}$ and electrophoretic force $\mathbf{F_e}$, $\boldsymbol{f} = \mathbf{F_{st}} + \mathbf{F_e}$. The phase interface formed by ionic liquid and air under an atmospheric environment can be represented by the isoline ($\phi = 0.5$) of the level set function: $\phi = 0$ in air and $\phi = 1$ in ionic liquid. Therefore, the level set function can be regarded as the volume fraction of ionic liquid. The transformation process of two phases at the interface can be described by

$$\frac{\partial \phi}{\partial t} + \boldsymbol{v}\cdot\nabla\phi = \gamma^*\nabla\cdot\left(\varepsilon\nabla\phi - \phi(1-\phi)\frac{\nabla\phi}{|\nabla\phi|}\right). \tag{2}$$

ε is the control parameter of interface thickness, γ^* is the reinitialized parameter, and the stability of numerical operation and interface quality can be controlled by adjusting these two parameters, which are generally empirical values ($\varepsilon = 15\ \mu$m $\gamma^* = 1$).

For the coupling characteristics of multi-physical fields, numerical simulation at the interface requires that the fluid density and viscosity should be smoothed by

$$\begin{cases} \rho = \rho_{air} + \left(\rho_{liquid} - \rho_{air}\right)\phi, \\ \mu = \mu_{air} + \left(\mu_{liquid} - \mu_{air}\right)\phi. \end{cases} \tag{3}$$

The surface tension is defined as

$$\mathbf{F_{st}} = \gamma\delta\kappa\mathbf{n}. \tag{4}$$

$\mathbf{n}$ is the normal vector of the interface $\left(\mathbf{n} = \frac{\Delta\phi}{|\nabla\phi|}\right)$, γ is the surface tension coefficient, κ is the curvature of the interface ($\kappa = -\nabla\cdot\mathbf{n}$), and δ is the Dirac function [$\delta = 6|\phi(1-\phi)||\nabla\phi|$].

The contact between the interface and the wall allows a small amount of slip, and the reasonable constraint of the wall on the fluid interface is realized by defining the boundary force $\mathbf{F_\alpha} = \mathbf{F_n} + \mathbf{F_r}$, where $\mathbf{F_n}$ is the normal pressure of the interface on the wall and $\mathbf{F_r}$ is the friction force generated by the slip. The specific definition is

$$\begin{aligned} \mathbf{F_n} &= \gamma\delta(\mathbf{n_{wall}}\cdot\mathbf{n} - \cos\theta_w)\mathbf{n}, \\ \mathbf{F_r} &= -\frac{\mu}{\beta}\boldsymbol{v}. \end{aligned} \tag{5}$$

$\mathbf{n_{wall}}$ is the normal vector to the wall, $\boldsymbol{v}\cdot\mathbf{n_{wall}} = 0$. Since PTFE, the material used in the capillary, has a contact angle close to 90° with the ionic liquid, the contact angle (θ_w) on the capillary side is set to 90°. Moreover, the surface of the emitter has excellent wettability to ionic liquid because of the roughness treatment. Hence, the contact angle (θ_w) on the emitter side is set to 1°. Generally, the slip length ($\beta = 21\ \mu$m) is the average value of the unit size after the computation domain is discretized.

$\mathbf{F_e}$ can be obtained by Maxwell's stress tensor method. Furthermore, the stress tensor of electrostatic field is defined as

$$F_{ei} = \oiint_S \sum_{j=1}^{3} T_{ij}\mathrm{d}S_j, \quad i = 1,2,3. \tag{6}$$

F_{ei} represents the component in one direction of the Coulomb force acting on the charge in plane S. T_{ij} is the Maxwell stress tensor element. In a Cartesian coordinate system, Eq. (6) can be expanded into a matrix form,

$$\begin{bmatrix} \mathrm{d}F_{ex} \\ \mathrm{d}F_{ey} \\ \mathrm{d}F_{ez} \end{bmatrix} = \begin{bmatrix} T_{xx} & T_{xy} & T_{xz} \\ T_{yx} & T_{yy} & T_{yz} \\ T_{zx} & T_{zy} & T_{zz} \end{bmatrix} \begin{bmatrix} \mathrm{d}S_x \\ \mathrm{d}S_y \\ \mathrm{d}S_z \end{bmatrix}. \tag{7}$$

Since F_{ei} acts on all charge elements in plane S, Eq. (6) can also be written as follows:

$$F_{ei} = \iiint_V f_{ei}\mathrm{d}V, \quad i = 1,2,3. \tag{8}$$

f_{ei} is the Coulomb force acting on the unit volume charge, which can be calculated by

$$\boldsymbol{f}_{\mathbf{e}} = \rho_{\mathrm{e}}\boldsymbol{E} = (\nabla \cdot \boldsymbol{D})\boldsymbol{E}. \tag{9}$$

ρ_{e} is the charge density. $\boldsymbol{D}$ is the electric displacement field, and $\boldsymbol{E}$ is the electrostatic field. By comparing Eqs. (6) and (8), according to the relation between the surface integral and volume integral, the following can be obtained:

$$f_{ei} = \sum_{j=1}^{3} \frac{\partial T_{ij}}{\partial x_j}. \tag{10}$$

$x_j(j = 1, 2, 3)$ stands for x, y, z in Cartesian coordinates. The following equation can be obtained from Eq. (9):

$$f_{ei} = \sum_{j=1}^{3} \varepsilon_0 \varepsilon_r E_i \frac{\partial E_j}{\partial x_j} = \sum_{j=1}^{3} \varepsilon_0 \varepsilon_r \left[\frac{\partial}{\partial x_j}(E_i E_j) - E_j \frac{\partial E_i}{\partial x_j} \right]. \tag{11}$$

ε_0 is the vacuum permittivity ($\varepsilon_0 = 8.8542 \times 10^{-12}\mathrm{F/m}$). ε_{r} is the relative dielectric constant of the ionic liquid.

The electrostatic field is irrotational, $\nabla \times \boldsymbol{E} = 0$,

$$\frac{\partial E_i}{\partial x_j} = \frac{\partial E_j}{\partial x_i}. \tag{12}$$

Substituting Eq. (12) into the second term at the right end of Eq. (11), the following equation can be obtained:

$$\begin{aligned} \sum_{j=1}^{3} E_j \frac{\partial E_i}{\partial x_j} &= \sum_{j=1}^{3} E_j \frac{\partial E_j}{\partial x_i} = \sum_{j=1}^{3} \frac{1}{2} \frac{\partial}{\partial x_i}(E_j E_j) \\ &= \frac{1}{2} \frac{\partial}{\partial x_i}(E^2) = \sum_{j=1}^{3} \frac{\partial}{\partial x_j} \left(\frac{1}{2}_{ij} E^2 \right). \end{aligned} \tag{13}$$

By substituting Eq. (13) into Eq. (11) and comparing with Eq. (10), the following equation can be obtained:

$$T_{ij} = \varepsilon_0 \varepsilon_{\mathrm{r}} \left(E_i E_j - \frac{1}{2} \delta_{ij} E^2 \right). \tag{14}$$

δ_{ij} is the Kronecker function,

$$\delta_{ij} = \begin{cases} 1, & i = j, \\ 0, & i \neq j, \end{cases} \qquad i, j = 1, 2, 3.$$

Rewriting Eq. (14) into a matrix form,

$$T = \frac{\varepsilon_0 \varepsilon_{\mathrm{r}}}{2} \begin{bmatrix} E_x^2 - E_y^2 - E_z^2 & 2E_x E_y & 2E_x E_z \\ 2E_y E_x & E_y^2 - E_z^2 - E_x^2 & 2E_y E_z \\ 2E_z E_x & 2E_z E_y & E_z^2 - E_x^2 - E_y^2 \end{bmatrix}. \tag{15}$$

By substituting Eq. (15) into Eq. (7), it is simplified to a two-dimensional problem. The expression of F_{ei} in the rectangular coordinate system can be obtained,

$$\begin{cases} \mathrm{F}_{ex} = \dfrac{\varepsilon_0 \varepsilon_{\mathrm{r}}}{2} \iiint_V \left[\dfrac{\mathrm{d}(E_x^2 - E_y^2)}{\mathrm{d}x} + \dfrac{\mathrm{d}(2E_x E_y)}{\mathrm{d}y} \right] dV, \\ \mathrm{F}_{ey} = \dfrac{\varepsilon_0 \varepsilon_{\mathrm{r}}}{2} \iiint_V \left[\dfrac{\mathrm{d}(2E_y E_x)}{\mathrm{d}x} + \dfrac{\mathrm{d}(E_y^2 - E_x^2)}{\mathrm{d}y} \right] dV. \end{cases} \tag{16}$$

The distribution of electrostatic field is obtained by solving Poisson's equations,

$$\begin{cases} \boldsymbol{D} = \varepsilon_0 \varepsilon^* E, \\ \boldsymbol{E} = -\nabla U, \\ \nabla \cdot \boldsymbol{D} = 0. \end{cases} \tag{17}$$

U is the voltage applied at the wall of the capillary. Meanwhile, ε^* is smoothed at the phase interface, as shown in Eq. (3),

$$\varepsilon^* = \frac{1}{2}[\varepsilon_{\mathrm{air}} + \varepsilon_{\mathrm{r}} + (\varepsilon_{\mathrm{r}} - \varepsilon_{\mathrm{air}})\phi]. \tag{18}$$

$\varepsilon_{\mathrm{air}}$ is the relative permittivity of air ($\varepsilon_{\mathrm{air}} = 1$).

As shown in Fig. 2, the numerical simulation process can be divided into three steps within one calculation cycle. In the first step, the volume fraction of two fluids and the initial phase interface can be obtained by solving Eq. (2) according to the initial conditions and boundary conditions of the electrostatic field, and the potential distribution can be obtained by solving Eq. (17) according to the initial conditions and boundary conditions of the electrostatic field. At this moment, both the surface tension $\mathbf{F}_{\mathbf{st}}$ and electrophoretic force $\mathbf{F}_{\mathbf{e}}$ can be calculated. In the second step, the velocity distribution can be obtained by solving Eq. (1) according to the initial conditions and boundary conditions of the flow field. In the third step, the velocity distribution is plugged into Eq. (2) to solve the new level set function (ϕ). Meanwhile, the convergence of the calculation results is judged by tolerance. If the calculation result is not convergent, the surface tension and electrophoretic force will be recalculated by the new level set function. It will be iterated until the calculation result is converged and output. The time terms are discretized by using backward difference. The calculation uses a full coupling method, which forms a large equation group for solving all unknown quantities or fields and contains all coupling among unknown quantities in one iteration. The numerical simulation adopts the Newton–Raphson method for iteration.

To sum up, the coupling among the electrostatic field, flow field, and level set function is realized. The electrowetting results of the variables are obtained by numerical solution. In addition, the configuration of the meniscus at each moment during the electrowetting process is also obtained so as to determine the threshold of initial wetting voltage and summarize the law about the electrowetting velocity and the liquid film thickness.

B. The diameter of extractor hole d_1

So as to obtain the electrowetting curve under the influence of each variable, the threshold of initial wetting voltage must be explored by applying bias ramp sweep voltage. On second thought, so as to eliminate the influence of liquid inertia force in the process of changing from the initial level to the stable meniscus, the voltage is applied after the phase interface reaches the stable meniscus. Therefore, the numerical calculation is divided into two parts. The first part is the threshold of initial wetting voltage obtained by bias ramp sweep voltage. The second part is to research the influence of various variables on the electrowetting curve when the threshold of initial wetting voltage is applied. As shown in Fig. 3, the first part is divided into three sections. AB is the process from initial level change to the stable meniscus. BC is the transition process of the phase interface in

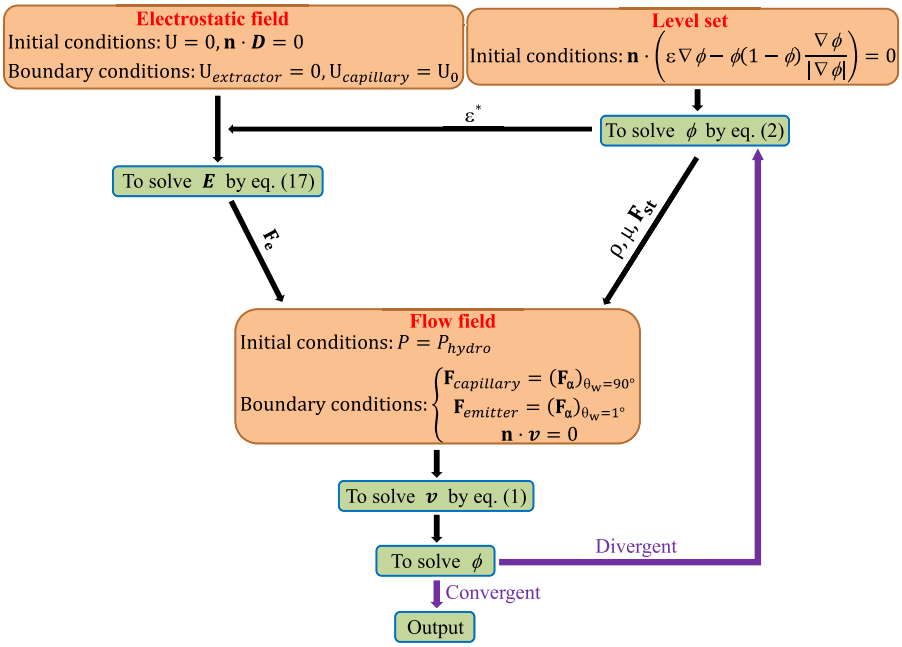

FIG. 2. Numerical simulation flowchart and field coupling.

the meniscus state. CD is the process of ionic liquid climbing along the emitter surface after applying bias ramp sweep voltage. The bias ramp sweep voltage is applied at point E, which comes from the time axis of section BC. It can be observed that the leading edge of the liquid climbs significantly at a certain voltage value (point C) and the corresponding voltage value at this point is the threshold of initial wetting voltage.

The value range of variable d_1 in the experiment is usually 0.2–0.5 mm. If $d_1 < 0.2$ mm, the beam current transmittance of the gate is extremely low. If $d_1 > 0.5$ mm, the divergence angle of the plume is widened, and the threshold of emission voltage will also increase, leading to aggravating the power consumption of the thruster. Therefore, the value of d_1 is adjusted to 0.2, 0.3, and 0.4 mm, which is representative for numerical calculation. As shown in Fig. 3, the wetting curves corresponding to different d_1 are almost completely overlapped in section AE because d_1 has no influence on the configuration of the free meniscus. After applying the bias ramp sweep voltage at point E, the electrowetting curve begins to differ in section CD. The three curves climb uniformly to point D with similar electrowetting velocity, indicating that variable d_1 has little influence on electrowetting.

As shown in Fig. 4, two tangents can be made to the same wetting curve and converge at a certain point in time. The voltage corresponding to the time point is the threshold of the initial wetting voltage U_0. U_0 corresponding to each d_1 is not very different. When the voltage is greater than 2000 V, the ionic liquid begins to climb along the emitter under the action of electrophoretic force.

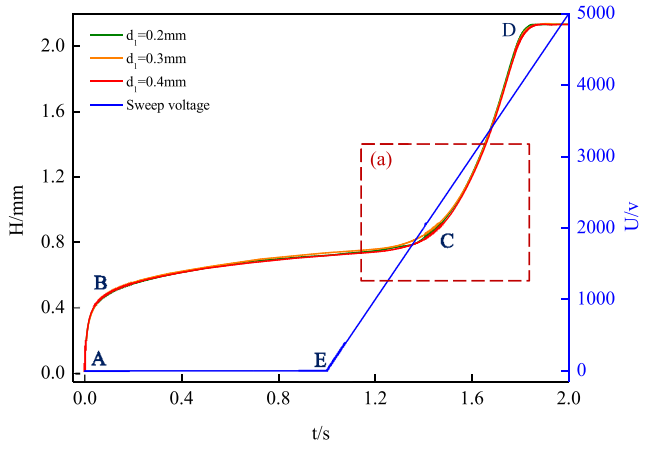

FIG. 3. d_2 = 0.2 mm, θ = 23.67° EMI-TFSI; the effect of d_1 on electrowetting.

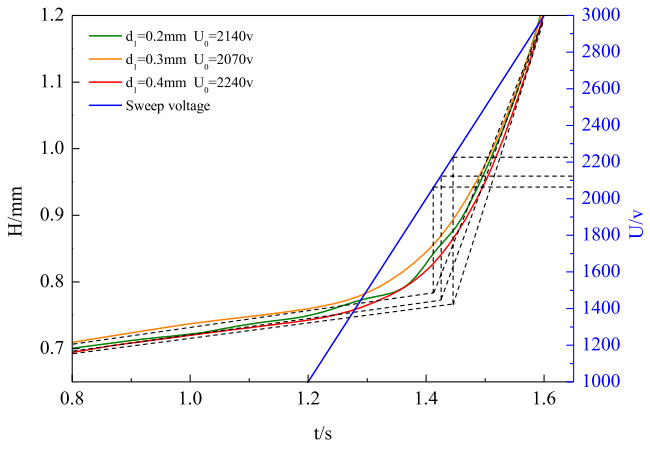

FIG. 4. A partial enlargement of the area (a) in Fig. 3.

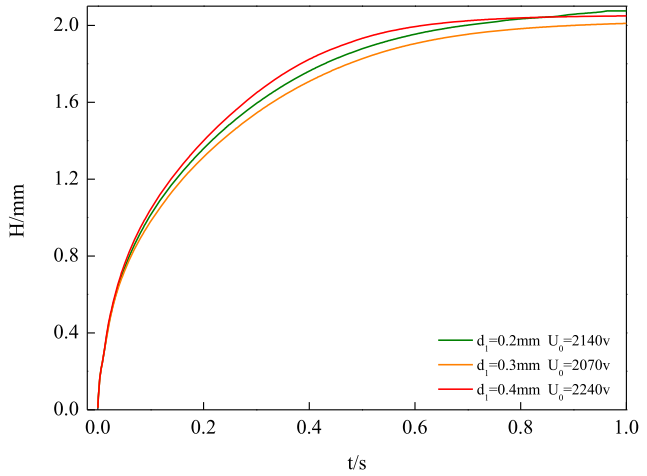

FIG. 5. Electrowetting curve of ionic liquid climbing along emitter at the threshold of wetting voltage.

As shown in Fig. 5, when the phase interface is at the initial position, the threshold of the initial wetting voltage corresponding to each d_1 is applied to obtain the corresponding electrowetting curve. In this condition, U_0 is the constant step voltage. Under the combined action of inertia force, viscous force, gravity, and electrophoretic force, the electrowetting velocity decreases gradually during the process of the liquid leading edge climbing along the emitter to the tip. Finally, the electrowetting velocity changes to 0 after reaching the tip. The variation rules of electrowetting curves corresponding to different d_1 are roughly similar, which proves once again that variable d_1 has little influence on electrowetting.

C. The distance from extractor to emitter d_2

As shown in Fig. 6, the section AB of each electrowetting curve is a process in which the phase interface changes freely in the absence of the electrostatic field. For section AE, the electrowetting curves

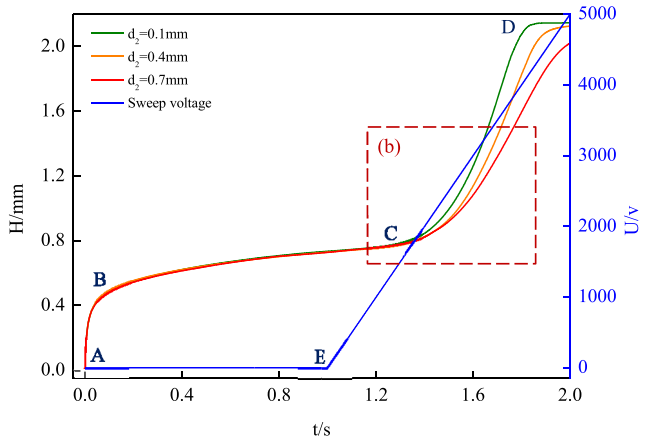

FIG. 6. d_1 = 0.5 mm, θ = 23.67° EMI-TFSI; the effect of d_2 on electrowetting.

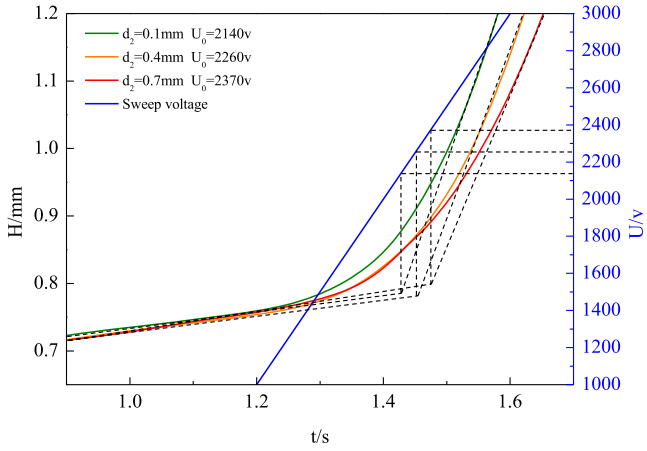

FIG. 7. A partial enlargement of the area (b) in Fig. 6.

corresponding to different d_2 almost completely coincide because variable d_2 has no influence on the configuration of the free meniscus. After the bias ramp sweep voltage is applied at point E, the electrowetting curve begins to differ in section CD. With the increase in d_2, the electrowetting velocity gradually decreases under the same voltage, and the time for the liquid leading edge to climb from the initial position to the tip along the emitter also becomes longer. After applying bias ramp scan voltage, the electrowetting velocity of each d_2 is uniform.

As shown in Fig. 7, the threshold of initial wetting voltage corresponding to each d_2 was obtained by enlarging and drawing the area near point C of the electrowetting curve. With the increase in d_2, the threshold of initial wetting voltage presents a monotonically increasing trend.

As shown in Fig. 8, when the phase interface is at the initial position, the threshold of initial wetting voltage corresponding to each d_2 is applied to obtain the electrowetting curve, and U_0 is set as the constant step voltage in this condition. With the increase in

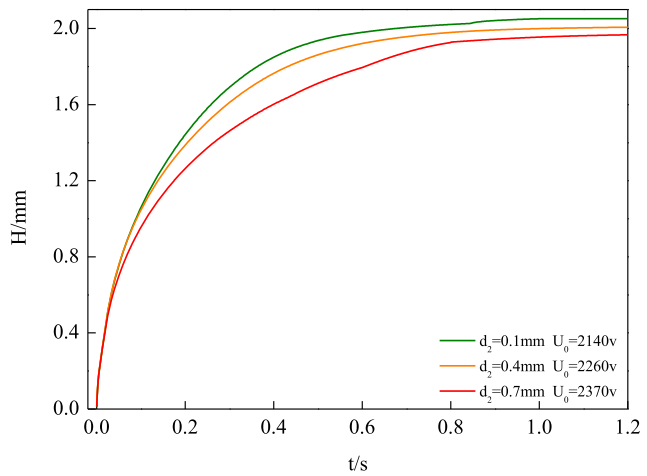

FIG. 8. Electrowetting curve of ionic liquid climbing along emitter at the threshold of wetting voltage.

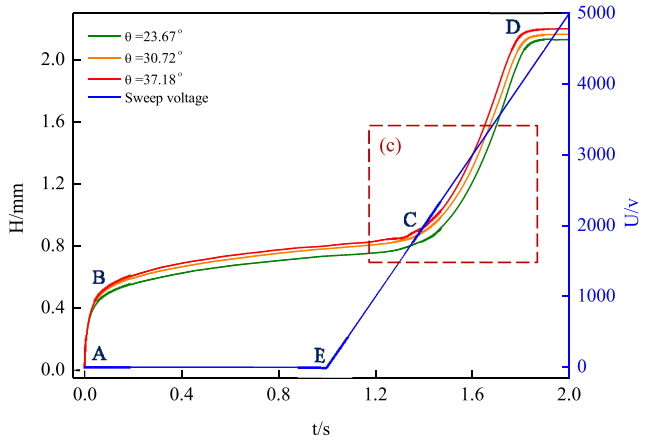

FIG. 9. d_1 = 0.5 mm, d_2 = 0.2 mm EMI-TFSI; the effect of θ on electrowetting.

d_2, the electrowetting velocity decreases at the same time, but the threshold increases. When the liquid leading edge at the emitter side climbs from the initial position to the tip, the electrowetting velocity corresponding to each d_2 gradually decreases, and the velocity becomes 0 when it reaches the tip.

D. The V-blade emitter angle θ

As shown in Fig. 9, the variable θ can influence the configuration of the free meniscus, so the wetting curves corresponding to each θ show differences in section AE. With the increase in θ, the climbing distance of ionic liquid along the emitter increases at the same time, and the electrowetting velocity does not change and is uniform. After the electrostatic field is applied at point E, the electrowetting curves corresponding to each θ continue to climb from the liquid leading edge of the stable meniscuses at the emitter side to the tip with the same electrowetting velocity.

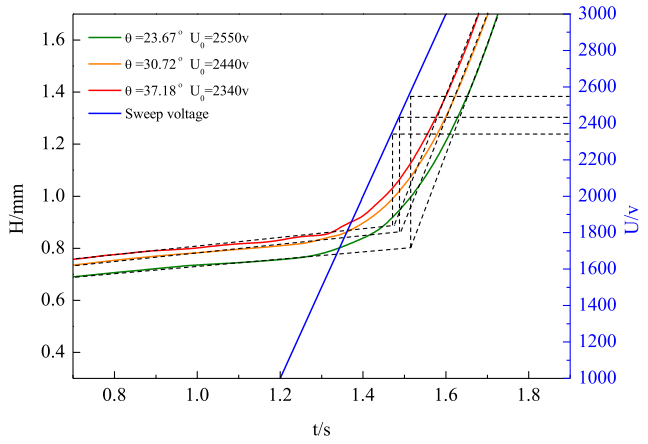

FIG. 10. Partial enlargement of area (c) in Fig. 9.

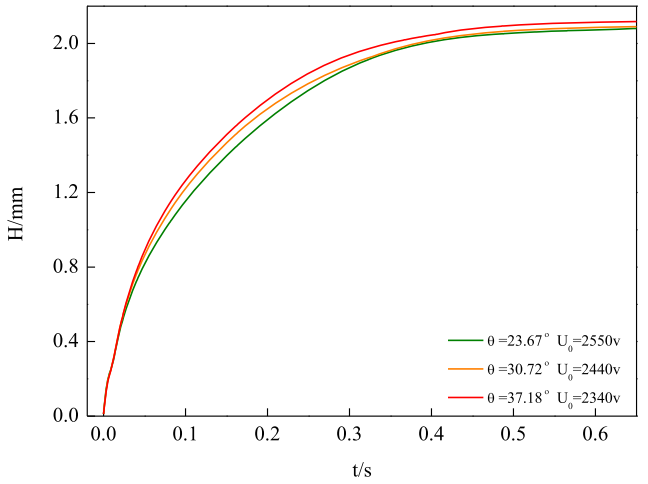

FIG. 11. Electrowetting curve of ionic liquid climbing along emitter at the threshold of wetting voltage.

As shown in Fig. 10, the threshold of initial wetting voltage corresponding to each θ is obtained by enlarging and drawing the area near point C of the wetting curve. With the increase in θ, the threshold presents a monotonically decreasing trend.

Figure 11 shows the wetting curve corresponding to each θ when the threshold of initial wetting voltage is applied. With the increase in θ, the electrowetting velocity increases at the same time, but the threshold decreases. When the liquid leading edge at the emitter side climbs from the initial position to the tip, the electrowetting velocity of each θ decreases gradually and becomes 0 when it reaches the tip. The initial liquid level height of all numerical models is maintained at 1.4 mm. During the calculation, the liquid mass is required to be conserved. The ionic liquid wets the emitter and spreads out into a thin film of uniform thickness. At the same time, the flow of ionic liquid at the tip reaches a static equilibrium, and the complete wetting of the emitter is achieved.

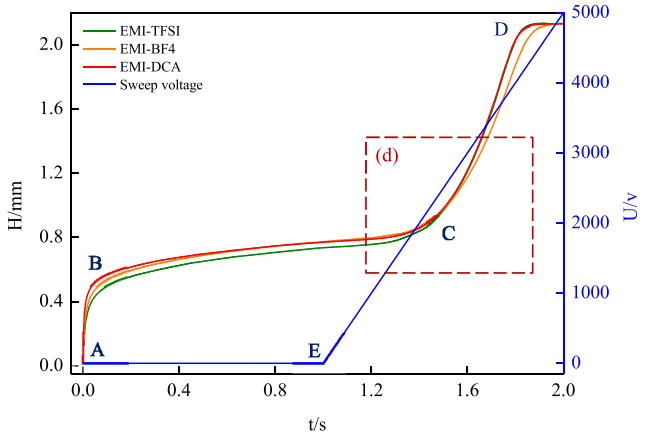

FIG. 12. d_1 = 0.5 mm, d_2 = 0.2 mm, and q = 23.67°; the effect of propellant on electrowetting.

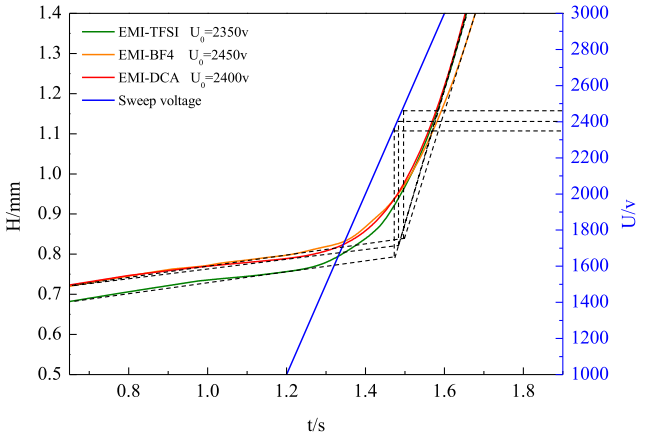

FIG. 13. Partial enlargement of area (d) in Fig. 12.

E. The physical properties of propellant

As shown in Fig. 12, the physical properties of ionic liquids have an impact on the configuration of the free meniscus, so the wetting curves corresponding to different ionic liquids show differences immediately in section AE. Because of the greater viscosity of EMI-BF_4, the electrowetting velocity is lower than that of EMI-TFSI and EMI-DCA, and it also takes longer to wet the tip of the emitter. After the electrostatic field is applied at point E, the liquid leading edge is disturbed by electrophoretic force, and phase interface becomes unbalanced. It begins to climb at a constant velocity after reaching the threshold of initial wetting voltage.

As shown in Fig. 13, the threshold of initial wetting voltage corresponding to each ionic liquid is obtained by magnifying and drawing the area near point C of the wetting curve. Due to the smaller surface tension of EMI-TFSI, the threshold is lower than that of EMI-BF_4 and EMI-DCA.

Figure 14 shows the corresponding wetting curves of each ionic liquid when the threshold of initial wetting voltage is applied.

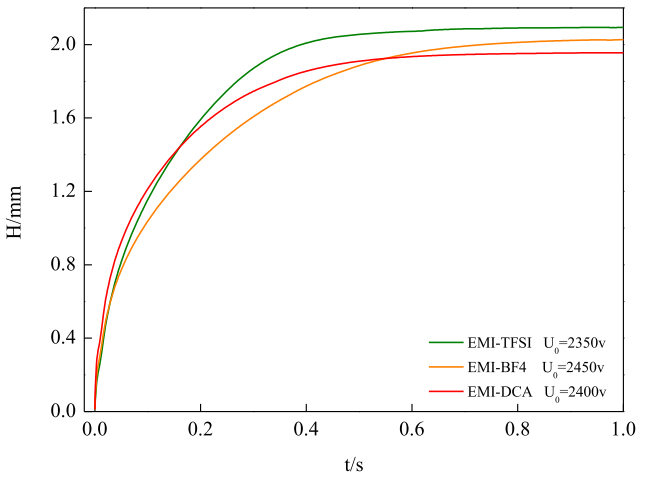

FIG. 14. Electrowetting curve of ionic liquid climbing along emitter at the threshold of wetting voltage.

Because EMI-TFSI has a smaller liquid viscosity, the electrowetting velocity is higher than that of EMI-BF_4 and EMI-DCA at the same time. In the process of the liquid leading edge at the emitter side climbing from the initial position to the tip, the electrowetting velocity of each ionic liquid gradually decreases to 0 when it reaches the tip.

IV. THE BEAM CURRENT EXPERIMENTAL RESULTS

As shown in Fig. 15, an emitter is a hybrid structure that consists of a pyramid emitter and a square capillary. The ILET has been fabricated by low-speed wire cutting combined with electrochemical etching.[21] Ions or ion clusters are ejected from the tip and fly into an electric-field-free region passing through a hole drilled coaxially on the extractor. These ions or ion clusters fly at a constant speed in a vacuum chamber and impinge on a metallic collector connected to a pico-ammeter, which can capture beam current.

A. The diameter of extractor hole d_1

The hybrid externally wetted ILET is tested for ignition and analyzed by intercepting the beam current data of 30 s when the positive and negative ions were stably emitted. Although the beam current I_b can be increased by increasing u^+ or u^- continuously, the emission current I_e will increase faster, which leads to the rapid decrease in beam current transmittance I_b/I_e. It means that the effective thrust and specific impulse are decreased while the power consumption increases. Simultaneously, excessive voltage will cause instant beam current loss stability, which shows strong nonlinearity in the $I_b - t$ diagram, indicating that there is a large thrust noise at this time. In contrast, if the voltage threshold for ion emission conditions is not reached, ions or ionic polymers cannot break through the energy barrier to form a stable beam current. In summary, in order to highlight the influence of key variables on the beam current, it is required to start collecting the beam current when the voltage threshold is applied, and at least stable ion emission can be formed.

As shown in Fig. 16, the diameter of the extractor hole has a great influence on the beam current transmittance. Regardless of pure anionic emission or pure cation emission, as the diameter of the extractor hole increases, the beam current increases, and the beam current transmittance also increases, which means that a larger aperture can obtain greater thrust when applying the same voltage. Because anions and cations have different charge mass ratios, anion emission and cationic emission have different emission voltage thresholds. The axial electric field intensity E_y is the main energy source for ionic liquid to break through the energy barrier. The increase in d_1 will weaken E_y at the liquid leading edge. The $I_b - t$ diagram shows that the increase in d_1 leads to the increase in emission voltage threshold u^+ or u^-.

When it is adjusted within the range of about 100 V above the emission voltage threshold, the beam current is in a stable emission mode with low noise. Under the same transmittance, a small increase in voltage of 1–10 V will increase the beam current by 1–60 nA. Considering the actual experimental situation, all $I_b - t$ diagrams cannot be completely and absolutely described as anionic beam current greater than cationic beam current or cationic beam current greater than anionic beam current but can show a small amplitude

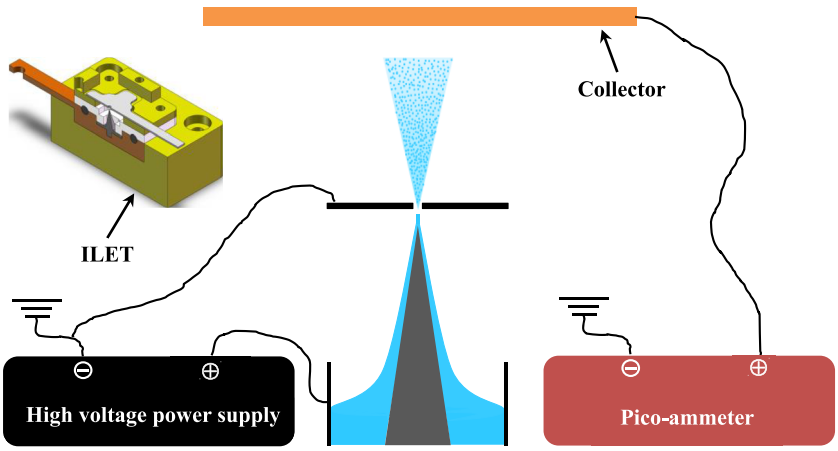

FIG. 15. Field emission testing system to detect beam current.

stable adjustment in a certain range that is greater than the emission voltage threshold. d_1 and d_2 have important influence on the thrust performance of an array ILET, so the experimental law about variables has important guiding significance for the optimization design of thruster ion optical systems.

B. The distance from extractor to emitter d_2

As shown in Fig. 17, d_2 has a great influence on the emission voltage threshold. With the increase in d_2, greater axial electric field intensity E_y is required to ensure that the ionic liquid can obtain enough energy to break through the constraint of the liquid interface, thus increasing the emission voltage threshold for maintaining stable jet flow. Theoretically, increasing d_2 can reduce the ion emission angle at the emitter tip, which is a simple and rough focusing method. When the power consumption of the thruster increases, the beam current decreases, and the beam current transmittance also decreases. Hence, a scheme for assembling a single grid cannot simultaneously meet the requirements of decreasing the divergence angle of the plume and increasing beam current transmittance. It is necessary to design a multi-grid ion optical system to focus the beam and improve the beam current transmittance. Thus, the thruster can have large beam current and a small divergence angle of the plume at the same time under low power consumption.

C. The V-blade emitter angle θ

As shown in Fig. 18, in order to highlight the influence of variable θ on beam current, it is necessary to ensure that the diameter of the emitter tip at different cone angles is within 5 μm in the experiment; then the beam current data under the influence of variable θ can be collected. If the meniscus is a free surface, there is an optimal conical angle that results in the best wettability or the fastest wettability. The best wettability and the fastest wettability cannot be obtained simultaneously.[17] Similarly, the meniscus in the electrostatic field has an optimal cone angle that maximizes the beam current and minimizes the voltage threshold for stable emission. As shown in Fig. 18, θ = 30.72°, meaning too large a cone angle will

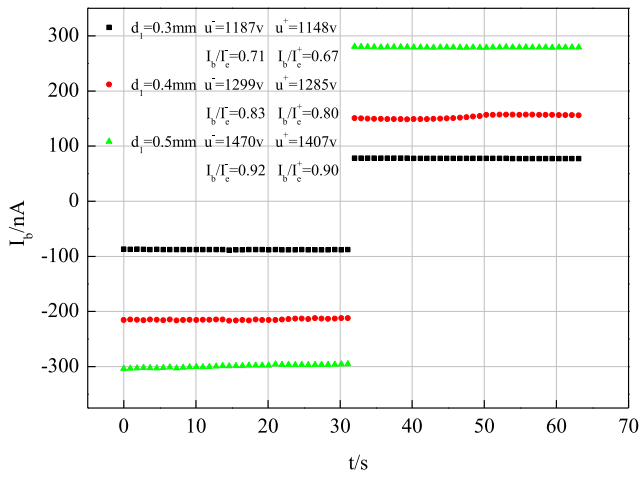

FIG. 16. d_2 = 0.2 mm, θ = 23.67° EMI-TFSI; the effect of d_1 on beam current.

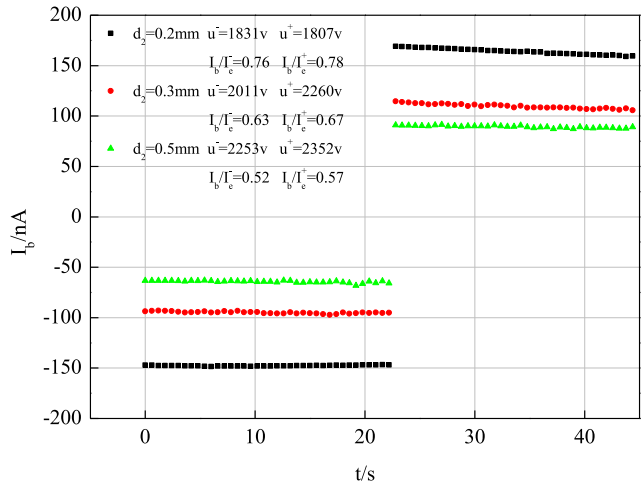

FIG. 17. d_1 = 0.4 mm, θ = 23.67° EMI-TFSI; the effect of d_2 on beam current.

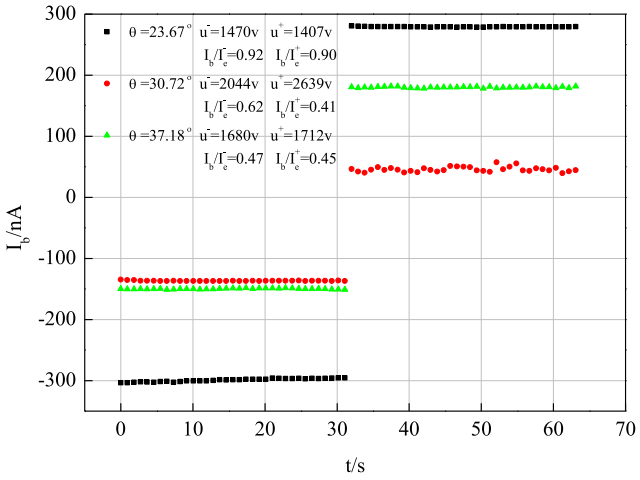

FIG. 18. d_1 = 0.5 mm, d_2 = 0.2 mm EMI-TFSI; the effect of θ on beam current.

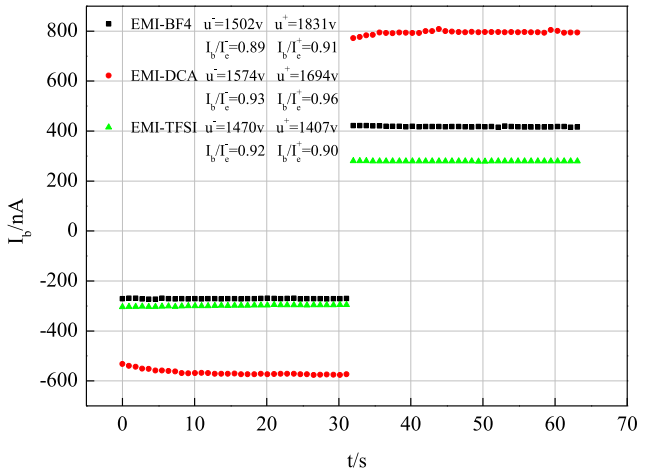

FIG. 20. d_1 = 0.5 mm, d_2 = 0.2 mm, and θ = 23.67°; the effect of propellant on beam current.

make the beam current and transmittance drop sharply, which will directly lead to most ions or ionic polymers being intercepted by the inner surface of the extractor, and cause sputtering corrosion on the inner surface of the extractor. A prolonged emission would also accelerate the damage around the extractor hole. In addition to this, the stability of beam current with too large a cone angle is poor, and it is difficult to form effective and stable thrust as well. The reason for this phenomenon may be that the emitter with excessive θ establishes multiple emission points at the tip. It is further explained that the coverage area of the strongest axial electric field E_y at the emitter tip increases, making the ion or ion polymer reach the energy threshold of ion emission at many points of the tip. As shown in Fig. 19, many scholars have observed the situation of multipoint emission in numerical simulation and even experiments, measured the small beam current and extremely low transmittance, and even photographed the serious sputtering corrosion on the gate surface caused by multipoint emission.

D. The physical properties of propellant

As shown in Fig. 20, the physical properties of ionic liquids have a great influence on beam current. Compared with EMI-BF_4 and EMI-TFSI, EMI-DCA has lower surface tension and viscosity, as well as high conductivity. These advantages make it easier for the anions and cations of EMI-DCA to break through the energy barrier with a lower emission voltage threshold and then escape from the liquid surface to form a stable beam current. At roughly the same beam current transmittance, the beam current of EMI-DCA is larger, indicating that it has a larger beam current density.

FIG. 19. Sputtering corrosion of the extractor caused by multipoint emission (d_1 = 0.5 mm).

E. The emitter material

As shown in Fig. 21, compared with the porous tungsten emitter, the externally wetted emitter has a larger beam current and beam current transmittance, as well as a lower emission voltage threshold. It can be interpreted that the exposed microchannel helps the tip

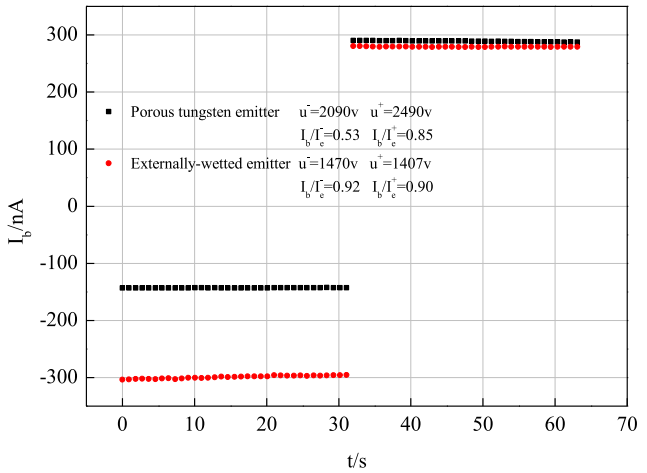

FIG. 21. d_1 = 0.5 mm, d_2 = 0.2 mm, θ = 23.67° EMI-TFSI; the effect of emitter material on beam current.

establish a stable cone jet in the electrostatic field. The microchannels on the emitter surface, processed by the etching process, extend from the bottom of the emitter to the tip, and multiple microchannels can ensure effective liquid supply. The microchannel can be cleaned by ultrasound to achieve good external wettability again even if it is blocked. The porous tungsten emitter increases the flow resistance due to its microscopic pore structure. Although it is easier to achieve pure ion emission, the continuous emission can very easily block the pore structure, resulting in the rapid decay of beam current and the reduction in ignition reliability, as shown in Fig. 22. The blockage is caused by the electrochemical reaction between the ionic liquid and emitter, and the reaction products are mostly floccule with high viscosity and easy crystallization. Even if periodic voltage with alternating polarity is applied to realize the alternating emission of anions and cations so as to delay the blockage, it is difficult to completely avoid the blockage. The microchannel of the externally wetted emitter is not easily blocked. Long life and low noise thrust can be produced by the ILET if a stable and high-resolution liquid supply is available. By contrast, the tip of the externally wetted emitter takes the place as a stable single point emission, while the tip of the porous tungsten emitter is an unstable multipoint emission. The blockage of the pore structure makes the emission more unstable, which is one of the reasons why the thrust noise of the porous tungsten thruster is very loud.

FIG. 22. Porous structure is blocked by electrochemical reaction products ($\theta = 23.67°$).

V. DISCUSSION

In order to study the hydrodynamics of ionic liquids in the electrostatic field, the interaction between fluid flow and potential distribution, the configuration of the meniscus during electrowetting, the distribution of polarized charge, and the force on the meniscus need to be discussed. A deep understanding of the electrowetting phenomenon is conducive to making accurate diagnosis when the performance of the ILET is abnormal.

The complete working process of the ILET can be divided into two independent physical stages. The first stage is electrowetting, where the ionic liquid is subjected to electrophoretic forces in an electrostatic field and climbs along the emitter surface to the tip. The second stage is field emission, where ions or ion clusters break through the energy barrier and escape from the phase interface under the charging of the electrostatic field. The first physical stage is simulated by numerical calculations in Sec. III, and the second physical stage is tested by beam current experiments in Sec. IV. We tried to build an experimental platform to observe the electrowetting by a high-speed camera. However, the actual testing environment ($\leq 4.5 \times 10^{-4}$ Pa) and the specific configuration of the emitter make the electrowetting experiment very difficult. In fact, the electrostatic field will change the contact angle (θ_w) between the ionic liquid and the wall so that the contact angle becomes a function of the electric potential field (U). The function could be described as θ_w (U) and measured by the electrowetting experiment.[22] The stronger bidirectional coupling between the flow field and the electrostatic field can be realized by adding this function as a boundary condition of the flow field in numerical simulation. However, the electrowetting experiment was not successfully carried out, so this function was ignored in the numerical simulation. Finally, the numerical simulation results in Sec. III cannot be verified by the electrowetting experiment. U_0 is the minimum voltage to achieve electrowetting, and u is the minimum voltage to achieve stable field emission. The most meaningful is the comparison and discussion between U_0 and u that the magnitude of u can be roughly determined by U_0. Hence, it provides a theoretical basis for the beam current experiment.

The threshold of initial wetting voltage (U_0) and the emission voltage threshold (u^+ or u^-) are two significant physical quantities. The power consumption of the thruster is directly determined by the emission voltage threshold, and the thrust power ratio is an important index to measure the working efficiency of the thruster. Theoretically, u should be slightly greater than U_0. U_0 is the minimum voltage that pulls the liquid leading edge to climb along the emitter in numerical calculation, and u is the minimum voltage required for the ion to break through the energy barrier to get rid of the phase interface binding in the emission test. It is necessary to analyze the reasons why u is less than U_0. First of all, according to the requirement of the emitter tip radius size, the smaller the tip radius ($<5\ \mu$m), the more conducive it is to the electrostatic field of evaporation and the maintaining the pure ion emission mode. The preparation technology requires a V-blade emitter to be changed as a pyramid emitter. As a result, the emission characteristic changes from a line to a point, which reduces the energy threshold for pure ion emission. Second, the microchannels etched on the pyramidal emitter surface reduce the contact angle ($\theta_w < 1°$) and enhance the capillary force of the ionic liquid climbing along the emitter. Finally,

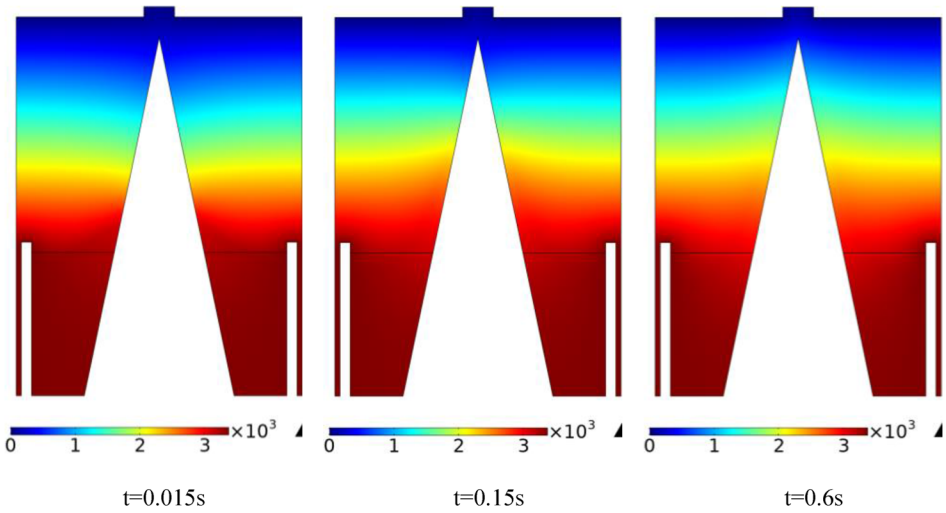

FIG. 23. d_1 = 0.3 mm, d_2 = 0.2 mm, θ = 23.67° EMI-TFSI; the configuration of meniscus affects the distribution of potential field (v). t = 0.015 s, t = 0.15 s, and t = 0.6 s.

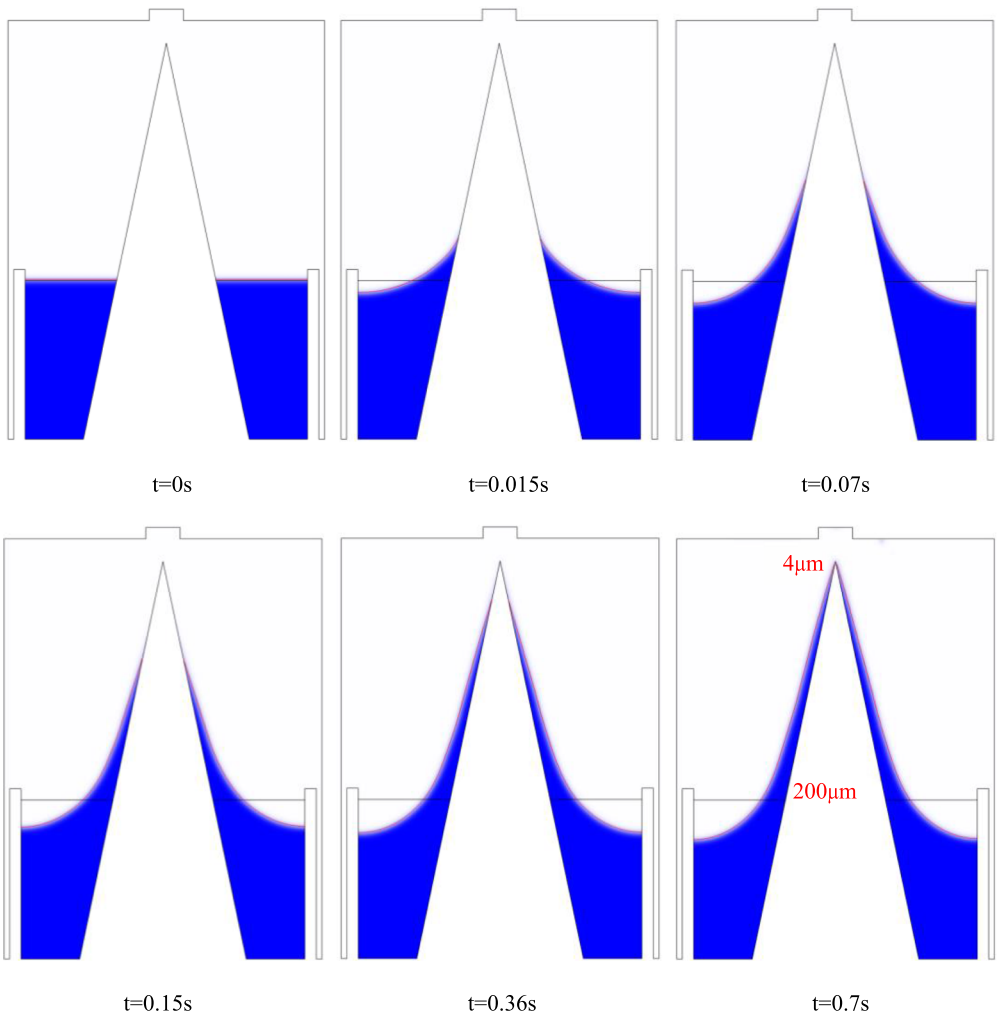

FIG. 24. d_1 = 0.3 mm, d_2 = 0.2 mm, θ = 23.67° EMI-TFSI; electrowetting process. t = 0 s, t = 0.015 s, t = 0.07 s, t = 0.15 s, t = 0.36 s, and t = 0.7 s.

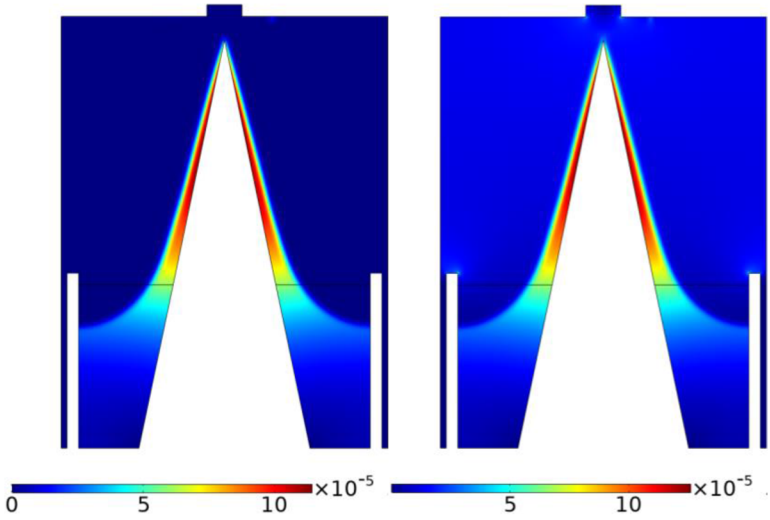

FIG. 25. d_1 = 0.3 mm, d_2 = 0.2 mm, θ = 23.67° EMI-TFSI; (a) the modulus of polarized charge (C/m^2); (b) the modulus of the electric displacement field (C/m^2). (a) t = 0.7 s and (b) t = 0.7 s.

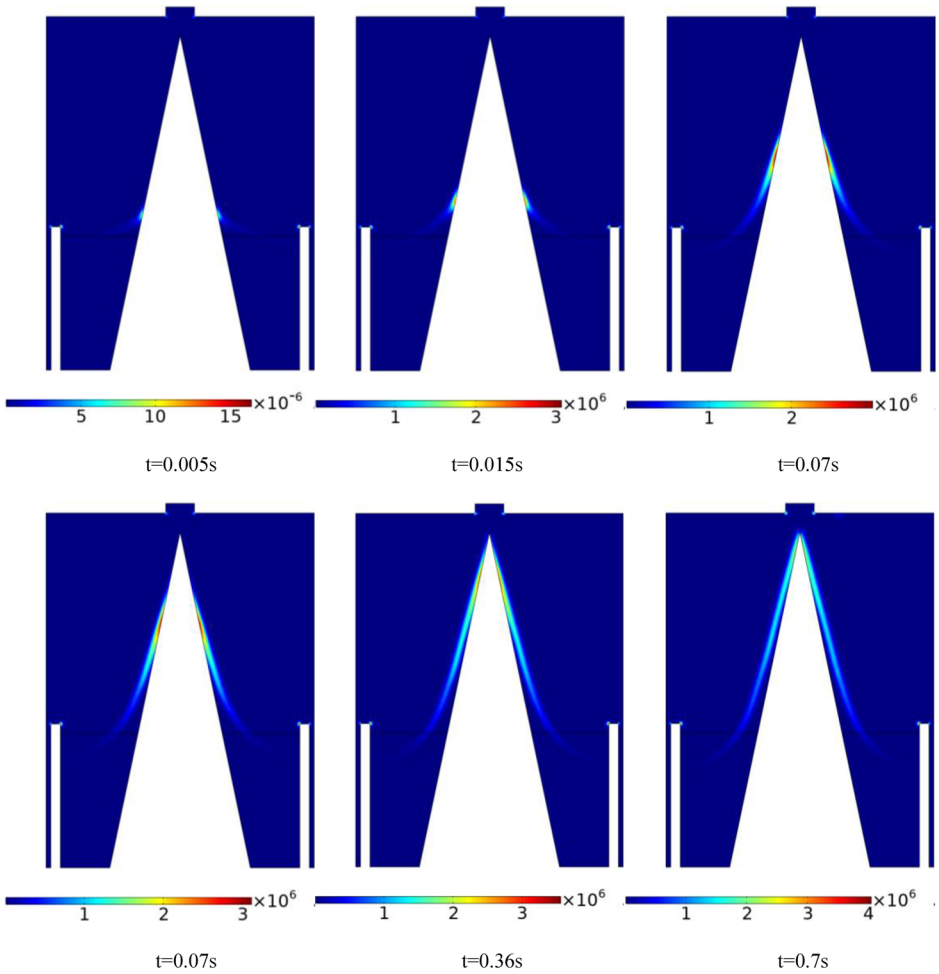

FIG. 26. d_1 = 0.3 mm, d_2 = 0.2 mm, θ = 23.67° EMI-TFSI; distribution of electrophoretic forces at different moments (N/m^3). t = 0.005 s, t = 0.015 s, t = 0.07 s. t = 0.07 s, t = 0.36 s, and t = 0.7 s.

the shape of the extractor hole is adjusted from a strip hole to a round hole, which changes the distribution of the electrostatic field. In summary, due to the adjustment of the thruster configuration and the requirements of the emitter preparation technology, the emission voltage threshold is less than the threshold of the initial wetting voltage, which is consistent with the results obtained in this paper. Regardless of using a V-blade emitter or pyramid emitter, the two-dimensional model is similar to the one shown in Fig. 1, so the rule summarized in numerical calculation is universal for the two kinds of emitters.

As shown in Fig. 23, a uniform electrostatic field is formed between the emitter and the extractor, and the configuration of the meniscus is different at different moments when the ionic liquid climbs along the emitter. The change in configuration leads to the change in electrostatic potential distribution. The results indicate that the bidirectional coupling of the electric field and flow field is realized by numerical calculation.

Figure 24 demonstrates the process of the liquid leading edge of the meniscus climbing from the initial position along the emitter to the tip and finally forming a liquid film with uniform thickness of 200–4 μm at the part of the V-blade emitter exposed to the capillary. Because the meniscus is subject to electrophoretic force, it no longer meets the assumption of a constant mean curvature surface, so the phenomena of infiltration relaxation and periodical infiltration oscillation do not occur during the electrowetting process.[17] The influence of the variables on the electrowetting velocity is reduced, but the threshold of the initial wetting voltage is greatly affected.

As shown in Fig. 25, polarized charges induced by the electrostatic field are distributed unevenly along the meniscus. The closer it is to the emitter tip, the more polarized the charge density is. As a consequence, the direction perpendicular to the emitter surface has a large gradient. A large number of polarized charges are mainly located at the bottom of the liquid layer.

As shown in Fig. 26, the electrophoretic force only acts on the phase interface and distributes unevenly along the meniscus. The closer it is to the emitter, the greater the electrophoretic force will be. As the liquid leading edge at the emitter side climbs, the area affected by electrophoretic force gradually expands to the whole meniscus. The maximum electrophoretic force at each moment is located at the leading edge of the emitter, which meets the requirement of ionic liquid continuously wetting the emitter.

VI. CONCLUSION

This article proposes a new hybrid emitter structure, which consists of a V-blade emitter and a square capillary. The effects of various variables on electrowetting and beam current characteristics are discussed, and it is proved that the hybrid emitter has great advantages such as sustaining a stable liquid supply and maintaining a pure ion emission mode. By analyzing the results of numerical calculation and experimental data, the complete laws about electrowetting velocity, the threshold of wetting voltage, liquid layer thickness, emission voltage threshold, beam current, and transmittance are summarized. The performance of the hybrid externally wetted ILET can be improved by design iteration of the thruster based on optimization of relevant variables.

The wettability of the hybrid externally wetted ILET is evaluated by numerical calculation. Besides, the ability of the hybrid emitter to form a continuous and stable liquid film in the electrostatic field to ensure liquid supply is verified. The electrowetting law of related variables has positive guiding significance to the optimization of the ILET. The possibility that the hybrid emitter can work normally and stably is proved by emission testing. The emission law of related variables lays a firm foundation for improving beam current and transmittance. To solve the problem that the emitter can be continuously wetted is the premise to ensure that the externally wetted ILET has stable, low noise and high thrust power ratio characteristics. The configuration of the hybrid emitter is conducive to the formation of a stable and continuous meniscus to ensure the integrity of the liquid film at the tip so as to maintain high efficiency of the pure ion emission mode.

ACKNOWLEDGMENTS

This work was supported by the Strategic Priority Research Program of the Chinese Academy of Science (Grant No. XDA1502110105) and the National Natural Science Foundation of China (Grant Nos. 12032020 and 12072354).

AUTHOR DECLARATIONS

Conflict of Interest

The authors have no conflicts to disclose.

DATA AVAILABILITY

The data that support the findings of this study are available from the corresponding author upon reasonable request.

REFERENCES

[1] C. Williams, S. DelPozzo, and B. Doncaster, *Nano/Microsatellite Market Forecast*, 9th ed. (Space Works Enterprises, Inc., 2019).
[2] P. L. Wright, H. Huh, N. M. Uchizono *et al.*, "A novel variable mode emitter for electrospray thrusters," in International Electric Propulsion Conference, 2019.
[3] V. Hruby *et al.*, "ST7-DRS colloid thruster system development and performance summary," in AIAA/ASME/SAE/ASEE Joint Propulsion Conference and Exhibit, 2008.
[4] N. R. Demmons, V. Hruby *et al.*, "Ground and on-orbit thruster performance comparison for the Lisa Pathfinder colloid micro-Newton thrusters," in 2018 Joint Propulsion Conference, 2018.
[5] J. Ziemer, M. Gamero-Castaño, V. Hruby *et al.*, "Colloid micro-Newton thruster development for the ST7-DRS and LISA missions," in AIAA/ASME/SAE/ASEE Joint Propulsion Conference and Exhibit, 2005.
[6] N. R. Demmons, D. Courtney, N. Alvarez *et al.*, "Component-level development and testing of a colloid micro-thruster (CMT) system for the LISA mission," in AIAA Propulsion and Energy 2019 Forum, 2019.
[7] M. Gamero-Castaño, R. E. Wirz *et al.*, "LISA colloid micro-thruster technology development plan and progress," in International Electric Propulsion Conference, 2019.
[8] Y. Chiu, G. Gaeta, T. R. Heine *et al.*, "Analysis of the electrospray plume from the EMI-Im propellant externally wetted on a tungsten needle," in AIAA/ASME/SAE/ASEE Joint Propulsion Conference and Exhibit, 2006.
[9] P. Lozano and M. Martínez-Sánchez, "Ionic liquid ion sources: Characterization of externally wetted emitters," J. Colloid Interface Sci. **282**(2), 415–421 (2005).

[10]B. Gassend, L. F. Velásquez-García *et al.*, "A fully microfabricated externally wetted electrospray thruster," in International Electric Propulsion Conference, 2007.
[11]B. R. Donius and J. L. Rovey, "Ionic liquid dual-mode spacecraft propulsion assessment," J. Spacecr. Rockets **48**(1), 110–123 (2011).
[12]T. Rexius and M. R. Holmes, "Mission capability gains from multi-mode propulsion thrust profile variations for a plane change maneuver," in AIAA Modeling and Simulation Conference, 2011.
[13]J. H. Gilland and S. R. Oleson, "Combined high and low thrust propulsion for fast piloted Mars missions," Final Contractor Report, Sverdrup Technology, Inc., Brook Park, OH, 1992.
[14]C. A. Kluever, "Spacecraft optimization with combined chemical-electric propulsion," J. Spacecr. Rockets **32**(2), 378–380 (1995).
[15]K. Masuyama and P. Lozano, "Bimodal propulsion system using ionic liquid propellant for pico- and nano-satellite applications," in AIAA/ASME/SAE/ASEE Joint Propulsion Conference and Exhibit, 2013.
[16]A. J. Mundahl, S. P. Berg, J. Rovey *et al.*, "Characterization of a novel ionic liquid monopropellant for multi-mode propulsion," AIAA/ASME/SAE/ASEE Joint Propulsion Conference and Exhibit, 2017.
[17]S. Xue, L. Duan, and Q. Kang, "Study on the emitter infiltration of needle-capillary ionic liquid electrospray thruster," AIP Adv. **11**(3), 035234 (2021).
[18]A. Kumar, "Salt effects on Diels–Alder reaction kinetics," Chem. Rev. **101**(1), 1 (2001).
[19]J. Fuller *et al.*, "The room temperature ionic liquid 1-ethyl-3-methylimidazolium tetrafluoroborate: Electrochemical couples and physical properties," J. Electrochem. Soc. **144**(11), 3881–3886 (1997).
[20]P. Lozano and M. Martínez-Sánchez, "Ionic liquid ion sources: Suppression of electrochemical reactions using voltage alternation," J. Colloid Interface Sci. **280**(1), 149–154 (2004).
[21]S. Xue, L. Duan, and Q. Kang, "Fabrication of externally wetted emitter for ionic liquid electrospray thruster by low-speed wire cutting combined with electrochemical etching," AIP Adv. **11**, 115023 (2021).
[22]J. Restolho, J. L. Mata, and B. Saramago, "Electrowetting of ionic liquids: Contact angle saturation and irreversibility," J. Phys. Chem. C **113**(21), 9321–9327 (2009).